Journal of Computational Physics 229 (2010) 4813–4830

Contents lists available at ScienceDirect

Journal of Computational Physics

journal homepage: www.elsevier.com/locate/jcp

A fully coupled 3-D mixed finite element model of Biot consolidation

Massimiliano Ferronato *, Nicola Castelletto, Giuseppe Gambolati

Dept. Mathematical Methods and Models for Scientific Applications, University of Padova, via Trieste 63, 35121 Padova, Italy

ARTICLE INFO

Article history:
Received 16 September 2009
Received in revised form 3 March 2010
Accepted 14 March 2010
Available online 17 March 2010

Keywords:
Mixed finite elements
Biot consolidation
Coupled solution

ABSTRACT

The numerical solution to the Biot equations of 3-D consolidation is still a challenging task because of the ill-conditioning of the resulting algebraic system and the instabilities that may affect the pore pressure solution. Recently new approaches have been advanced based on mixed formulations. In the present paper a fully coupled 3-D mixed finite element model is developed with the aim at alleviating the pore pressure numerical oscillations at the interface between materials with different permeabilities. A solution algorithm is implemented that takes advantage of the block structure of the discretized problem. The proposed model is verified against well-known analytical solutions and successfully experimented with in realistic applications of soil consolidation.

1. Introduction

Poro-elasticity denotes the coupled process between mechanics and flow in porous media. Its theoretical basis goes back to the mid 1920s when Terzaghi described analytically the one-dimensional (1-D) consolidation of a soil column under a constant load [1]. In 1941 Biot generalized Terzaghi's theory to three-dimensional (3-D) porous media [2] by establishing the mathematical framework which is usually termed as poro-elasticity. Even though sophisticated, and perhaps more elegant, approaches have been recently advanced, e.g. [3], the Biot equations of consolidation are still used today in a great variety of fields, ranging from reservoir engineering to biomechanics. For example, poro-elasticity is the basic theory to predict the compaction of a producing hydrocarbon reservoir and the related hazards, including land subsidence and borehole damages [4–6]. Several environmental issues connected with groundwater withdrawal, e.g. [7], or the safe long-term disposal of wastes in the subsurface, e.g. [8], can be addressed with the aid of poro-elastic models. In biomechanics the poro-elastic theory is used to describe tumor-induced stresses in the brain [9] and the bone deformation under a mechanical load [10].

Despite the intensive research in the area, the numerical solution to the Biot partial differential equations is still a challenging task for a number of reasons. First, the fully coupled approach leads to algebraic systems which can be quite difficult to solve, with the number of unknowns easily growing up to several hundreds of thousands in real 3-D applications. Second, the coefficient matrix resulting from the numerical discretization can be severely ill-conditioned especially at the early stage of the process [11], hence advanced preconditioners and solvers are needed to handle the fully coupled system [12,13]. Another approach relies on the iteratively coupled scheme which solves separately in a staggered way the mechanical and the fluid flow models until convergence. If sufficiently tight convergence criteria are prescribed, the iteratively coupled solution can be as accurate as the fully coupled one, but the number of required steps might be prohibitively high. Moreover, convergence of the iterative procedure is not always guaranteed depending on the fluid and soil mechanical properties [14].

* Corresponding author. Tel.: +39 049 8271332; fax: +39 049 8271333.
E-mail address: ferronat@dmsa.unipd.it (M. Ferronato).
URL: http://www.dmsa.unipd.it/~ferronat (M. Ferronato).

0021-9991/$ - see front matter © 2010 Elsevier Inc. All rights reserved.
doi:10.1016/j.jcp.2010.03.018

A third challenge is related to different forms of instabilities suffered by the numerical solution. For example, if an advection-dominated thermal process is associated to the Biot equations spurious oscillations may arise in the temperature and pressure fields because of sharp transient gradients [15]. However, the origin of most instabilities is due to the assumption that at the initial conditions the soil skeleton behaves as an incompressible medium if the pore fluid is so. Prescribing the volume change rate to be initially zero leads to the finite element (FE) pathology known as locking, which typically causes an oscillatory numerical behaviour in the pore pressure. In practice, such an occurrence takes place even if the fluid compressibility is different from zero but small enough with respect to the bulk compressibility. This form of instability appears at times smaller than a critical bound depending on the porous medium permeability and stiffness [16]. Different remedies can be implemented to cope with such numerical difficulty. For example, Reed [17] observed that using a different approximation order for displacement and pressure may help keep the spurious oscillations under control. In particular the pore pressure should be computed with the same approximation order as the stress, i.e. one order below the displacement, leading to FEs characterized by a linear pressure and a quadratic displacement. Unfortunately, such FEs typically provide a less accurate prediction of the soil deformation [18] with the oscillations in the pore pressure not entirely eliminated [19]. Post-processing techniques intended to smooth the spurious modes have been proposed with the aim at restoring the standard FE convergence rate [17,20]. More recently some approaches have been advanced based on mixed formulations. The main advantage from the mixed approximation spaces relies on the possibility of solving nearly incompressible problems with no locking and a greater flexibility in describing independently pressures, stresses and displacements. Tchonkova et al. [21] have developed a least-square mixed model for poro-elasticity yielding a positive definite discrete problem, while Phillips and Wheeler [22–24] have shown the theoretical convergence of two-dimensional (2-D) models that couple both continuous and discontinuous Galerkin elements for the displacements with mixed spaces for the fluid flow. A locally mass conservative approach coupling a mixed method for the flow problem with traditional FEs for the soil displacements has been proposed by Jha and Juanes [25] who suggest solving the overall model by an unconditionally stable sequential scheme.

In the present paper a fully coupled 3-D mixed FE formulation is developed to solve numerically the Biot equations of consolidation with the aim at alleviating the instabilities in the pore pressure solution. The fluid pore pressure and flux are approximated in the lowest order Raviart–Thomas mixed space, while linear tetrahedral FEs are used for the displacements. The main reasons for the above choices are threefold. First, keeping the flux as a primary variable allows for a greater accuracy in the velocity field, which can be of interest whenever a consolidation model is coupled with an advection–diffusion equation, e.g. to account for thermal effects or contaminant transport. Second, a mixed formulation for the flow problem is element-wise mass conservative because the normal flux is continuous across the element boundaries. Third, the practical advantages from using low-order interpolation elements, such as ease of implementation, refinement, and discretization of geometrically complex and heterogeneous domains, are thoroughly preserved. The paper is organized as follows. After a brief review of the governing partial differential equations, the mixed variational formulation is developed in a 3-D setting with the discrete system of ordinary differential equations integrated in time. A fully coupled algorithm is then derived, using the symmetric quasi-minimal residual (SQMR) solver [26] accelerated by a block preconditioner. The mixed FE model is verified against the well-known Terzaghi's (1-D) and Mandel's (2-D) analytical solutions and compared to the results obtained from a standard FE method, with the relative merits discussed. Finally, the proposed model is tested in two large-size realistic and numerically challenging applications with a few remarks closing the paper.

2. Mixed FE model of Biot consolidation

The interaction between a granular material and the fluid filling its pores is governed by a stress equilibrium equation coupled to a mass balance equation, with the relationship linking the grain forces to the fluid pore pressure based on Terzaghi's effective stress principle. The equilibrium equation for an isotropic poro-elastic medium incorporating the effective stress concept reads:

$$\mu\nabla^2\hat{\mathbf{u}} + (\lambda+\mu)\nabla\mathrm{div}\hat{\mathbf{u}} = \alpha\nabla p + \mathbf{b} \tag{1}$$

where λ and μ are the Lamé constants, α is the Biot coefficient, $\mathbf{b}$ the body forces, $\hat{\mathbf{u}}$ the medium displacements and p the fluid pore pressure. The fluid mass balance is prescribed by the continuity equation:

$$\mathrm{div}\mathbf{v} + \frac{\partial}{\partial t}(\phi\beta p + \alpha\,\mathrm{div}\hat{\mathbf{u}}) = f \tag{2}$$

where ϕ is the medium porosity, β the fluid compressibility, t time, f a flow source or sink and $\mathbf{v}$ Darcy's velocity. Eq. (2) must be coupled with Darcy's law defining $\mathbf{v}$:

$$\bar{\boldsymbol{\kappa}}^{-1}\mathbf{v} + \nabla p = 0 \tag{3}$$

with $\bar{\boldsymbol{\kappa}} = \bar{\mathbf{k}}/(\rho g)$, $\bar{\mathbf{k}}$ the hydraulic conductivity tensor and (ρg) the fluid specific weight.

Eqs. (1)–(3) form a coupled partial differential system defined on a 3-D domain Ω bounded by the frontier Γ with $\hat{\mathbf{u}}$, $\mathbf{v}$ and p as unknowns. This system can be solved with appropriate boundary:

$$\begin{cases} \hat{\mathbf{u}}(\mathbf{x},t) = \hat{\mathbf{u}}_D(\mathbf{x},t) & \text{over } \Gamma_D \\ \bar{\boldsymbol{\sigma}}_{\text{tot}}(\mathbf{x},t)\mathbf{n}(\mathbf{x}) = \mathbf{t}_N(\mathbf{x},t) & \text{over } \Gamma_N \\ p(\mathbf{x},t) = p_D(\mathbf{x},t) & \text{over } \Gamma_p \\ \mathbf{v}(\mathbf{x},t)\cdot\mathbf{n}(\mathbf{x}) = q_N(\mathbf{x},t) & \text{over } \Gamma_q \end{cases} \tag{4}$$

and initial conditions:

$$\begin{cases} \hat{\mathbf{u}}(\mathbf{x},0) = \hat{\mathbf{u}}_0(\mathbf{x}) \\ p(\mathbf{x},0) = p_0(\mathbf{x}) \end{cases} \tag{5}$$

In Eqs. (4) and (5) $\Gamma_D \cup \Gamma_N = \Gamma_p \cup \Gamma_q = \Gamma$, $\bar{\boldsymbol{\sigma}}_{\text{tot}}$ is the total stress tensor, $\mathbf{n}$ the outer normal to Γ and $\mathbf{x}$ the position vector in $\mathbb{R}^3$, while the right-hand sides are known functions.

2.1. Variational formulation

The partial differential system (1)–(3) with boundary conditions (4) and initial conditions (5) is solved numerically using a variational formulation. The unknown functions $\hat{\mathbf{u}}$, p and $\mathbf{v}$ are found in an appropriate space such that the integral form of (1)–(3) is satisfied for all test functions belonging to the corresponding space. The medium displacement $\hat{\mathbf{u}}(\mathbf{x},t)$ is approximated in the space generated by the continuous piecewise linear polynomials ℓ_i, $i = 1,\ldots,n_n$, with n_n the number of FE nodes in Ω:

$$\hat{\mathbf{u}}(\mathbf{x},t) = \begin{bmatrix} \hat{u}_x(\mathbf{x},t) \\ \hat{u}_y(\mathbf{x},t) \\ \hat{u}_z(\mathbf{x},t) \end{bmatrix} \simeq \begin{bmatrix} \sum_{i=1}^{n_n} \ell_i(\mathbf{x}) u_{x,i}(t) \\ \sum_{i=1}^{n_n} \ell_i(\mathbf{x}) u_{y,i}(t) \\ \sum_{i=1}^{n_n} \ell_i(\mathbf{x}) u_{z,i}(t) \end{bmatrix} = N_u(\mathbf{x})\mathbf{u}(t) \tag{6}$$

The fluid pore pressure $p(\mathbf{x},t)$ and Darcy's velocity $\mathbf{v}(\mathbf{x},t)$ are represented in the piecewise constant polynomial and lowest order Raviart–Thomas space, respectively, thus satisfying the LBB condition that ensures the well-posedness of the discrete problem [27]. Denoting by n_e and n_f the number of elements and faces, respectively, we set:

$$p(\mathbf{x},t) \simeq \sum_{j=1}^{n_e} h_j(\mathbf{x}) p_j(t) = \mathbf{h}^T(\mathbf{x})\mathbf{p}(t) \tag{7}$$

$$\mathbf{v}(\mathbf{x},t) \simeq \sum_{k=1}^{n_f} \mathbf{w}_k(\mathbf{x}) q_k(t) = W(\mathbf{x})\mathbf{q}(t) \tag{8}$$

where h_j are element-wise constant functions:

$$h_j(\mathbf{x}) = \begin{cases} 1 & \mathbf{x} \in T^{(j)} \\ 0 & \mathbf{x} \in \Omega - T^{(j)} \end{cases} \tag{9}$$

and $\mathbf{w}_k$ are vectorial functions in $\mathbb{R}^3$ associated to the kth face belonging to the jth tetrahedron $T^{(j)}$:

$$\mathbf{w}_k(\mathbf{x}) = \begin{cases} \pm \frac{(\mathbf{x}-\mathbf{x}_k)}{3|V(T^{(j)})|} & \mathbf{x} \in T^{(j)} \\ \mathbf{0} & \mathbf{x} \in \Omega - T^{(j)} \end{cases} \tag{10}$$

with V the volume of $T^{(j)}$ and $\mathbf{x}_k$ the position vector of the node opposite to the kth face in $T^{(j)}$. The ± sign in (10) identifies a conventional face orientation such that $\mathbf{w}_k$ points outward the element $T^{(j)}$ with the smallest index j. Because of this orientation, the function $\mathbf{w}_k$ gives rise to a unitary flux through the kth face and a null flux through all other faces. Eq. (10) implies that $\mathbf{w}_k$ is not zero over the tetrahedrons sharing the kth face and is discontinuous across it. Continuity of $\mathbf{w}_k$ is ensured only along the normal direction relative to the kth face. The vectors $\mathbf{u}(t)$, $\mathbf{p}(t)$ and $\mathbf{q}(t)$ whose components are the nodal displacements $u_{x,i}$, $u_{y,i}$, $u_{z,i}$, $i = 1,\ldots,n_n$, the elemental pressures p_j, $j = 1,\ldots,n_e$, and the face normal fluxes q_k, $k = 1,\ldots,n_f$, respectively, are the discrete unknowns of the variational problem.

A weak form of the coupled system (1)–(3) is obtained using the classical approaches followed in both elasto-statics and fluid-dynamics. As for Eq. (1), the integral form is found by minimizing the total potential energy in the domain Ω with the aid of the virtual work principle:

$$\int_\Omega \boldsymbol{\epsilon}^{v,T} \boldsymbol{\sigma}_{\text{tot}} \, \mathrm{d}\Omega = \int_\Omega \hat{\mathbf{u}}^{v,T} \mathbf{b} \, \mathrm{d}\Omega + \int_{\Gamma_N} \hat{\mathbf{u}}^{v,T} \mathbf{t}_N \, \mathrm{d}\Gamma \tag{11}$$

where, according to the classical Voigt notation [28], $\boldsymbol{\epsilon}$ is the strain vector ($= [\epsilon_x, \epsilon_y, \epsilon_z, \gamma_{xy}, \gamma_{yz}, \gamma_{xz}]^T = B_u\mathbf{u}$, with B_u the strain elastic matrix) and $\boldsymbol{\sigma}_{\text{tot}}$ is the total stress vector ($= [\sigma_{x,\text{tot}}, \sigma_{y,\text{tot}}, \sigma_{z,\text{tot}}, \tau_{xy,\text{tot}}, \tau_{yz,\text{tot}}, \tau_{xz,\text{tot}}]^T$). The apex v denotes the virtual variables. Recalling Terzaghi's principle:

$$\boldsymbol{\sigma}_{\text{tot}} = \boldsymbol{\sigma} - \alpha p \mathbf{i} \tag{12}$$

where $\boldsymbol{\sigma}$ is the effective stress vector ($= [\sigma_x, \sigma_y, \sigma_z, \tau_{xy}, \tau_{yz}, \tau_{xz}]^T = D_e \boldsymbol{\epsilon}$, with D_e the elastic constant matrix) and $\mathbf{i}$ the Kronecker delta in vectorial form, and differentiating with respect to the virtual displacements, Eq. (11) yields:

$$\left(\int_\Omega B_u^T D_e B_u \, \mathrm{d}\Omega \right) \mathbf{u} - \int_\Omega \alpha B_u^T \mathbf{i} p \, \mathrm{d}\Omega = \int_\Omega N_u^T \mathbf{b} \, \mathrm{d}\Omega + \int_{\Gamma_N} N_u^T \mathbf{t}_N \, \mathrm{d}\Gamma \tag{13}$$

Introducing the pore pressure approximation (7) into (13) produces the final discrete form of Eq. (1):

$$K\mathbf{u} - Q\mathbf{p} = \mathbf{f}_1 \tag{14}$$

where

$$K = \int_\Omega B_u^T D_e B_u \, \mathrm{d}\Omega \tag{15}$$

$$Q = \int_\Omega \alpha B_u^T \mathbf{i} \mathbf{h}^T \, \mathrm{d}\Omega \tag{16}$$

$$\mathbf{f}_1 = \int_\Omega N_u^T \mathbf{b} \, \mathrm{d}\Omega + \int_{\Gamma_N} N_u^T \mathbf{t}_N \, \mathrm{d}\Gamma \tag{17}$$

The Dirichlet boundary conditions along Γ_D are prescribed in a strong way.

The integral form of Eqs. (2) and (3) is obtained by a standard Galerkin approach. Using the approximations (6)–(8) gives:

$$\int_\Omega \mathbf{h} \mathrm{div} \mathbf{v} \, \mathrm{d}\Omega + \int_\Omega \mathbf{h} \frac{\partial \phi \beta p}{\partial t} \, \mathrm{d}\Omega + \int_\Omega \mathbf{h} \frac{\partial \alpha \mathrm{div} \hat{\mathbf{u}}}{\partial t} \, \mathrm{d}\Omega = \int_\Omega \mathbf{h} f \, \mathrm{d}\Omega \tag{18}$$

$$\int_\Omega W^T \bar{\boldsymbol{\kappa}}^{-1} \mathbf{v} \, \mathrm{d}\Omega + \int_\Omega W^T \nabla p \, \mathrm{d}\Omega = 0 \tag{19}$$

Assuming that ϕ, β and α are independent of time and using a weak form for the last integral in Eq. (19), the semi-discrete mixed FE expression of Eqs. (2) and (3) read:

$$B^T \mathbf{q} + P\dot{\mathbf{p}} + Q^T \dot{\mathbf{u}} = \mathbf{f}_2 \tag{20}$$

$$A\mathbf{q} - B\mathbf{p} = \mathbf{f}_3 \tag{21}$$

where

$$A = \int_\Omega W^T \bar{\boldsymbol{\kappa}}^{-1} W \, \mathrm{d}\Omega \tag{22}$$

$$B = \int_\Omega \boldsymbol{\omega} \mathbf{h}^T \mathrm{d}\Omega \tag{23}$$

$$P = \int_\Omega \phi \beta \mathbf{h} \mathbf{h}^T \, \mathrm{d}\Omega \tag{24}$$

$$\mathbf{f}_2 = \int_\Omega \mathbf{h} f \, \mathrm{d}\Omega \tag{25}$$

$$\mathbf{f}_3 = -\int_{\Gamma_p} p_D W^T \mathbf{n} \, \mathrm{d}\Gamma \tag{26}$$

The components of $\boldsymbol{\omega}$ in (23) are equal to $\mathrm{div}(\mathbf{w}_k)$, $k = 1, \ldots, n_f$. Unlike standard FEs, the Dirichlet boundary conditions are the natural conditions for Eq. (21) and are therefore prescribed in a weak way, whereas the Neumann boundary conditions are to be imposed in a strong way.

2.2. Numerical implementation

The system of differential-algebraic equations (14), (20) and (21) is numerically integrated in time by a finite difference scheme. Consider any time-dependent function to vary linearly in time between t and $t + \Delta t$, and approximate any time-derivative at the intermediate instant τ:

$$\tau = \theta(t + \Delta t) + (1 - \theta)t \tag{27}$$

by a first-order incremental ratio. In Eq. (27) θ is a scalar value comprised between 0 and 1. The discrete solution scheme thus obtained is the following:

$$\theta\left[K\mathbf{u}^{t+\Delta t}-Q\mathbf{p}^{t+\Delta t}\right]=(1-\theta)\left[Q\mathbf{p}^{t}-K\mathbf{u}^{t}+\mathbf{f}_1^{t}\right]+\theta\mathbf{f}_1^{t+\Delta t} \tag{28}$$

$$\frac{Q^T\mathbf{u}^{t+\Delta t}+P\mathbf{p}^{t+\Delta t}}{\Delta t}+\theta B^T\mathbf{q}^{t+\Delta t}=(1-\theta)\left[\mathbf{f}_2^{t}-B^T\mathbf{q}^{t}\right]+\frac{Q^T\mathbf{u}^{t}+P\mathbf{p}^{t}}{\Delta t}+\theta\mathbf{f}_2^{t+\Delta t} \tag{29}$$

$$\theta[A\mathbf{q}^{t+\Delta t}-B\mathbf{p}^{t+\Delta t}]=(1-\theta)\left[B\mathbf{p}^{t}-A\mathbf{q}^{t}+\mathbf{f}_3^{t}\right]+\theta\mathbf{f}_3^{t+\Delta t} \tag{30}$$

where the initial values used for $\mathbf{q}$ are consistent with the initial pressure space distribution $p_0(\mathbf{x})$. Set $\gamma=\theta\Delta t$ and $\psi=(1-\theta)/\theta$, divide Eq. (28) by $-\theta$, multiply Eq. (29) by Δt and Eq. (30) by $-\Delta t$. The numerical solution at time $t+\Delta t$ can be therefore computed by solving a linear algebraic system:

$$\mathcal{A}\mathbf{z}^{t+\Delta t}=\mathbf{f}^{t} \tag{31}$$

where

$$\mathcal{A}=\begin{bmatrix}P & Q^T & \gamma B^T\\ Q & -K & 0\\ \gamma B & 0 & -\gamma A\end{bmatrix}\quad \mathbf{z}^{t+\Delta t}=\begin{bmatrix}\mathbf{p}^{t+\Delta t}\\ \mathbf{u}^{t+\Delta t}\\ \mathbf{q}^{t+\Delta t}\end{bmatrix}\quad \mathbf{f}^{t}=\begin{bmatrix}\mathbf{f}^{(p)}\\ \mathbf{f}^{(u)}\\ \mathbf{f}^{(q)}\end{bmatrix} \tag{32}$$

$$\mathbf{f}^{(p)}=(\Delta t-\gamma)\left[\mathbf{f}_2^{t}-B^T\mathbf{q}^{t}\right]+Q^T\mathbf{u}^{t}+P\mathbf{p}^{t}+\gamma\mathbf{f}_2^{t+\Delta t} \tag{33}$$

$$\mathbf{f}^{(u)}=\psi\left[K\mathbf{u}^{t}-Q\mathbf{p}^{t}-\mathbf{f}_1^{t}\right]-\mathbf{f}_1^{t+\Delta t} \tag{34}$$

$$\mathbf{f}^{(q)}=(\Delta t-\gamma)\left[A\mathbf{q}^{t}-B\mathbf{p}^{t}-\mathbf{f}_3^{t}\right]-\gamma\mathbf{f}_3^{t+\Delta t} \tag{35}$$

The matrix $\mathcal{A}$ in (31) has size $n_e+3n_n+n_f$ and is sparse, symmetric and indefinite. Suitable solvers for (31) belong to the class of the iterative projection-type Krylov subspace methods properly preconditioned. The explicit construction of $\mathcal{A}$, however, is generally not convenient from a computational point of view. In fact, while A, B, K, P and Q can be computed just once at the beginning of the simulation as they do not depend on t, $\mathcal{A}$ changes at each step because Δt, hence γ, can be generally increased as the consolidation proceeds. Therefore, a specific block version of a preconditioned Krylov subspace method is to be implemented.

As far as the preconditioner is concerned, we develop a variant of the block constraint approach successfully applied to standard FE consolidation models [12,13]. Write $\mathcal{A}$ as a 2×2 block matrix:

$$\mathcal{A}=\begin{bmatrix}P & H^T\\ H & -C\end{bmatrix} \tag{36}$$

with:

$$H=\begin{bmatrix}Q\\ \gamma B\end{bmatrix}\quad C=\begin{bmatrix}K & 0\\ 0 & \gamma A\end{bmatrix} \tag{37}$$

Note that C is a block-diagonal symmetric positive definite (SPD) matrix, as both K and A are SPD and γ is positive. Now consider the following $\mathcal{A}$ decomposition:

$$\mathcal{A}=\begin{bmatrix}I & 0\\ HP^{-1} & I\end{bmatrix}\begin{bmatrix}P & 0\\ 0 & -S\end{bmatrix}\begin{bmatrix}I & P^{-1}H^T\\ 0 & I\end{bmatrix} \tag{38}$$

where S is the SPD Schur complement:

$$S=C+HP^{-1}H^T=\begin{bmatrix}K+QP^{-1}Q^T & \gamma QP^{-1}B^T\\ \gamma BP^{-1}Q^T & \gamma A+\gamma^2BP^{-1}B^T\end{bmatrix} \tag{39}$$

Eqs. (38) and (39) could be computed exactly as P is diagonal, however S turns out to be much less sparse than C, hence it is convenient to drop some of its blocks. A simple approximation relies on prescribing the dropped S to preserve the same block-diagonal structure as C:

$$S\simeq\widetilde{S}=\begin{bmatrix}\widetilde{S}_1 & 0\\ 0 & \widetilde{S}_2\end{bmatrix}=\begin{bmatrix}K+QP^{-1}Q^T & 0\\ 0 & \gamma A+\gamma^2BP^{-1}B^T\end{bmatrix} \tag{40}$$

The blocks $\widetilde{S}_1$ and $\widetilde{S}_2$ cannot be efficiently inverted, so an additional approximation is performed by replacing them with their incomplete Cholesky factorizations:

$$\widetilde{S}\simeq\begin{bmatrix}L_{S1}L_{S1}^T & 0\\ 0 & L_{S2}L_{S2}^T\end{bmatrix}=L_SL_S^T \tag{41}$$

$\widetilde{S}$ is used in Eq. (38) in place of the exact Schur complement S, thus providing a factored approximation of $\mathcal{A}$ that can be used as preconditioner. Inverting Eq. (38) and accounting for (41) yields:

$$\mathcal{M}^{-1} = \mathcal{U}^{-1}\mathcal{L}^{-1} = \begin{bmatrix} I & -P^{-1}H^T L_S^{-T} \\ 0 & L_S^{-T} \end{bmatrix} \begin{bmatrix} P^{-1} & 0 \\ L_S^{-1}HP^{-1} & -L_S^{-1} \end{bmatrix} \tag{42}$$

with $\mathcal{M}^{-1}$ the block constraint preconditioner (CP). The algorithm for applying $\mathcal{M}^{-1}$ to a vector $\mathbf{r}$:

$$\mathbf{s} = \mathcal{M}^{-1}\mathbf{r} \Rightarrow \begin{bmatrix} \mathbf{s}_1 \\ \mathbf{s}_2 \end{bmatrix} = \begin{bmatrix} I & -P^{-1}H^T L_S^{-T} \\ 0 & L_S^{-T} \end{bmatrix} \begin{bmatrix} P^{-1} & 0 \\ L_S^{-1}HP^{-1} & -L_S^{-1} \end{bmatrix} \begin{bmatrix} \mathbf{r}_1 \\ \mathbf{r}_2 \end{bmatrix} \tag{43}$$

is provided in Table 1.

The preconditioner (42) is used to accelerate the SQMR solver [26] which has proved a robust and efficient algorithm for sparse symmetric indefinite problems, e.g. [29,30]. The resulting complete CP-SQMR algorithm for the solution of equations (31) is provided in Appendix A. The repeated solution of Eq. (31) starting from the initial conditions (5) gives the discrete vectors $\mathbf{u}$, $\mathbf{p}$ and $\mathbf{q}$ at the selected values of time, hence the approximate $\hat{\mathbf{u}}$, p and $\mathbf{v}$ through Eqs. (6)–(8), respectively.

3. Numerical results

The stability and accuracy of the 3-D mixed FE consolidation model previously described is investigated with the aid of a few examples. First, the model is verified against 1-D and 2-D analytical solutions. Then, it is compared to a standard FE model. Finally, two realistic engineering applications are briefly addressed.

3.1. Model verification

The model is verified against both Terzaghi's (1-D) and Mandel's (2-D) consolidation problems.

Terzaghi's problem [1] consists of a fluid-saturated column of height L with a constant loading P_L on top (Fig. 1). Drainage is allowed for through the upper moving boundary only. The basement is fixed. The load is applied instantaneously at time $t = 0$ yielding a non-zero initial overpressure $p_0(z)$ and a corresponding settlement $u_0(z)$. Assuming the z-axis positive downward, the analytical solution reads [31,32]:

$$p(z,t) = \frac{4}{\pi}p_0 \sum_{m=0}^{\infty} \frac{1}{2m+1} \exp\left[\frac{-(2m+1)^2\pi^2 ct}{4L^2}\right] \sin\left[\frac{(2m+1)\pi z}{2L}\right] \tag{44}$$

$$u(z,t) = c_M p_0 \left\{ (L-z) - \frac{8L}{\pi^2} \sum_{m=0}^{\infty} \frac{1}{(2m+1)^2} \exp\left[\frac{-(2m+1)^2\pi^2 ct}{4L^2}\right] \cos\left[\frac{(2m+1)\pi z}{2L}\right] \right\} + u_0 \tag{45}$$

where

$$p_0(z) = \frac{\alpha M}{K_u + 4\mu/3} P_L \tag{46}$$

$$u_0(z) = \frac{1}{K_u + 4\mu/3} P_L (L-z) \tag{47}$$

with $M = [\phi\beta + (\alpha-\phi)c_{br}]^{-1}$ the Biot modulus, c_{br} the solid grain compressibility, $K_u = \lambda + 2\mu/3 + \alpha^2 M$ the undrained bulk modulus, $c_M = (\lambda + 2\mu)^{-1}$ the vertical uniaxial compressibility, and $c = k/[\rho g(M^{-1} + \alpha^2 c_M)]$ the consolidation coefficient. A homogeneous sandy column with unit section and $L = 15$ m is simulated, with the relevant hydraulic and mechanical properties given in Table 2. The prescribed distributed load P_L is 10^4 Pa. The column is discretized into regular tetrahedrals with a characteristic element size $h = 0.5$ m (Fig. 1). The time integration is performed with a first-order implicit scheme ($\theta = 1$) and a constant time step $\Delta t = 0.1$ s. The simulation proceeds until steady state conditions are attained. A good matching be-

Table 1
CP application to a vector.

1.	$\mathbf{z}_1 = P^{-1}\mathbf{r}_1$
2.	$\mathbf{t} = H\mathbf{z}_1$
3.	$\mathbf{t} \leftarrow \mathbf{t} - \mathbf{r}_2$
4.	$\mathbf{z}_2 = L_S^{-1}\mathbf{t}$
5.	$\mathbf{s}_2 = L_S^{-T}\mathbf{z}_2$
6.	$\mathbf{y} = H^T\mathbf{s}_2$
7.	$\mathbf{s}_1 = P^{-1}\mathbf{y}$
8.	$\mathbf{s}_1 \leftarrow \mathbf{z}_1 - \mathbf{s}_1$

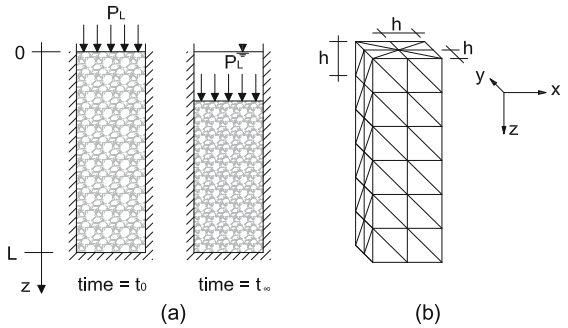

Fig. 1. Sketch of the setup for Terzaghi's consolidation test: (a) 1-D physical problem and (b) numerical discretization.

Table 2
Hydraulic and mechanical parameters of the porous medium used for the model verification. In Terzaghi's and Mandel's consolidation tests the sample is made from sand only.

	Porous medium
k_{sand} (m/s)	10^{-5}
k_{clay} (m/s)	10^{-8}
ϕ	0.375
β (MPa^{-1})	4.4×10^{-4}
λ (MPa)	40
μ (MPa)	40
α	1.0

tween the analytical and the numerical solution is obtained for both pore pressure and vertical displacement, as is shown in Figs. 2 and 3, respectively.

Mandel's problem [33] consists of a poroelastic slab sandwiched between two rigid, frictionless, and impermeable plates, both loaded by a constant vertical force as shown in Fig. 4. The slab is infinitely long in the y-direction with a $2a \times 2b$ wide cross-section. The outer surfaces ($x = \pm a$) are traction-free and drained. The load $2F$, i.e. a force per unit length in the y-direction, is suddenly applied at $t = 0$, causing both an instantaneous overpressure $p_0(x,z)$ and settlement $u_{x,0}(x,z)$ and $u_{z,0}(x,z)$, namely [34]:

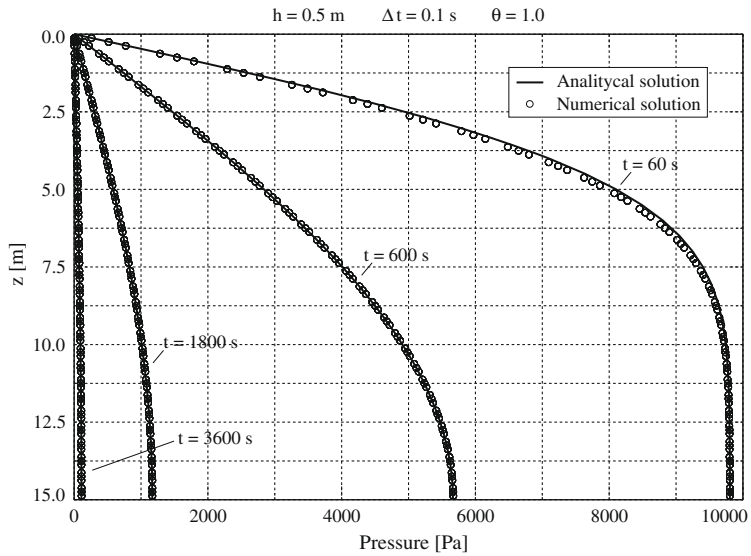

Fig. 2. Terzaghi's consolidation test: analytical and numerical solutions for the pore pressure.

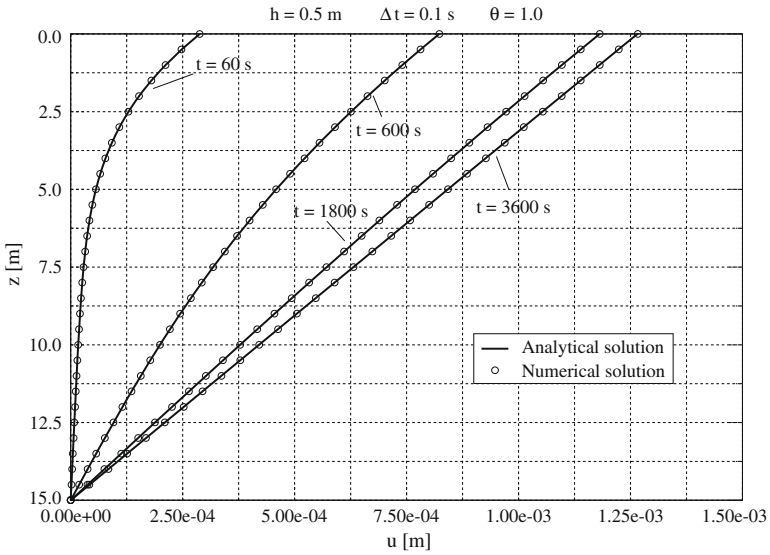

Fig. 3. Terzaghi's consolidation test: analytical and numerical solutions for the vertical displacement.

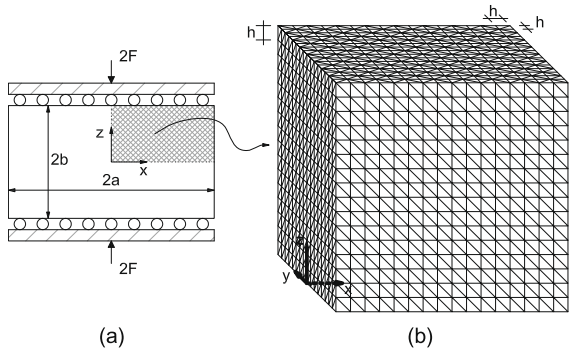

Fig. 4. Sketch of the setup for Mandel's problem: (a) 2-D physical problem after [34] and (b) numerical discretization.

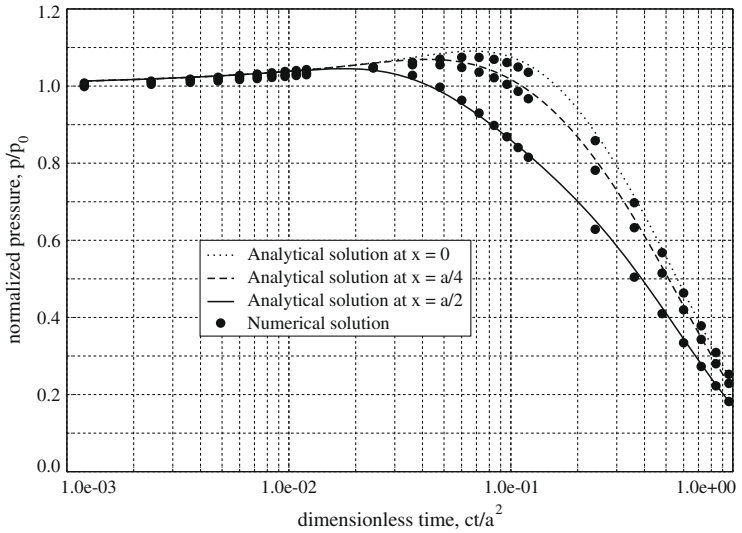

Fig. 5. Mandel's problem: pore pressure history at $x = 0$, $x = a/4$, and $x = a/2$.

$$p_0(x,z) = \frac{1}{3a} B(1+\nu_u) F \tag{48}$$

$$u_{x,0}(x,z) = \frac{F\nu_u}{2\mu}\frac{x}{a} \tag{49}$$

$$u_{z,0}(x,z) = -\frac{F(1-\nu_u)}{2\mu}\frac{y}{a} \tag{50}$$

with $B = \alpha M/K_u$ Skempton's coefficient, and $\nu_u = [3\nu + \alpha B(1-2\nu)]/[3 - \alpha B(1-2\nu)]$ and ν the undrained and drained Poisson's ratio, respectively. The analytical solution for the pore pressure reads [34]:

$$p(x,z,t) = 2p_0 \sum_{n=1}^{\infty} \frac{\sin\alpha_n}{\alpha_n - \sin\alpha_n \cos\alpha_n} \left(\cos\frac{\alpha_n x}{a} - \cos\alpha_n\right) \exp\left(\frac{-\alpha_n^2 ct}{a^2}\right) \tag{51}$$

where α_n are the positive roots of the nonlinear equation:

$$\tan\alpha_n = -\frac{\nu}{\nu_u - \nu}\alpha_n \tag{52}$$

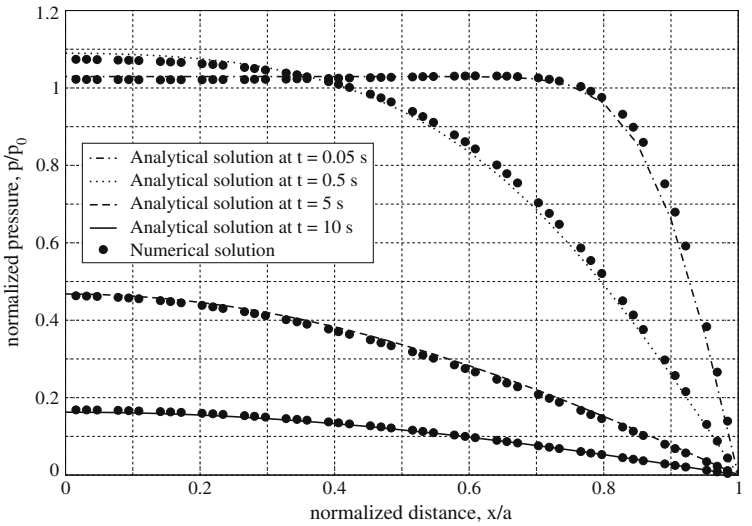

Fig. 6. Mandel's problem: pore pressure profile along the *x*-axis at various times.

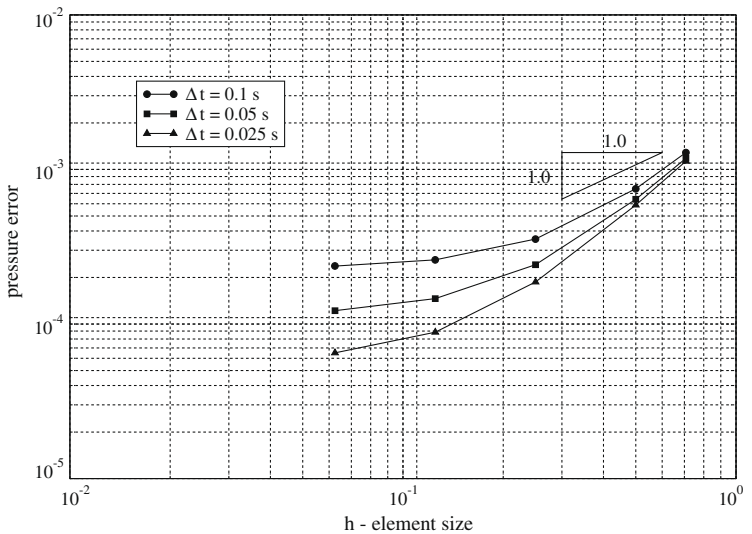

Fig. 7. Terzaghi's consolidation test: L^∞ pressure error norm vs. spacing *h*.

A homogeneous and isotropic slab is simulated using $a = b = 1$ m and the properties given in Table 2. F is set equal to 10^4 N/m. The domain symmetry allows for limiting the study to a quarter only of the x–z plane (Fig. 4). The 2-D problem is solved using a 3-D cube as domain with appropriate boundary conditions to warrant a plane strain condition along the y-direction [35]. A regular tetrahedral grid and an implicit $(\theta = 1)$ integration in time are used, with $h = 0.0625$ m and $\Delta t = 0.01$ s. The pore pressure vs. time and space is provided in Figs. 5 and 6, respectively, and shows a good agreement between the analytical and the numerical solution. Notice the peculiar non-monotonic pressure behaviour, i.e. the so-called Mandel–Cryer effect, with p rising above the initial p_0 at small time values because of the slab contraction at the drained faces inducing an additional build-up in the interior.

The convergence properties of the 3D mixed FE model have been investigated by comparing the analytical solutions (44) and (45) of Terzaghi's consolidation problem at $t = 60$ s with the numerical solution obtained on progressively refined computational grids, ranging from $h = 1$ m to 0.0625 m. In Fig. 7 the L^∞-norm of the pressure error is plotted vs. h in a double log–log plot using a constant Δt value for each profile. An initially linear behaviour can be noticed, then convergence tends to deteriorate as h decreases. The flattening portion of each profile is less pronounced as Δt is reduced. This agrees with the theoretical results provided in [23] for a 1-D formulation, with the lack of convergence for any given Δt due to the time dis-

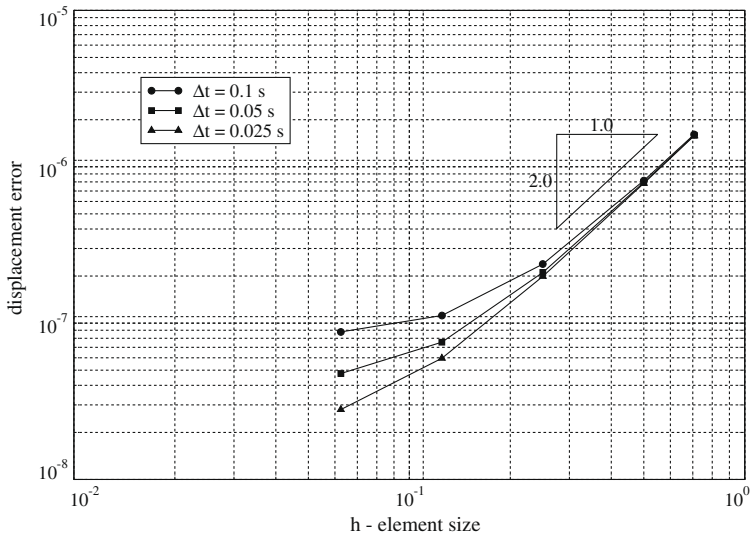

Fig. 8. Terzaghi's consolidation test: L^2 displacement error norm vs. spacing h.

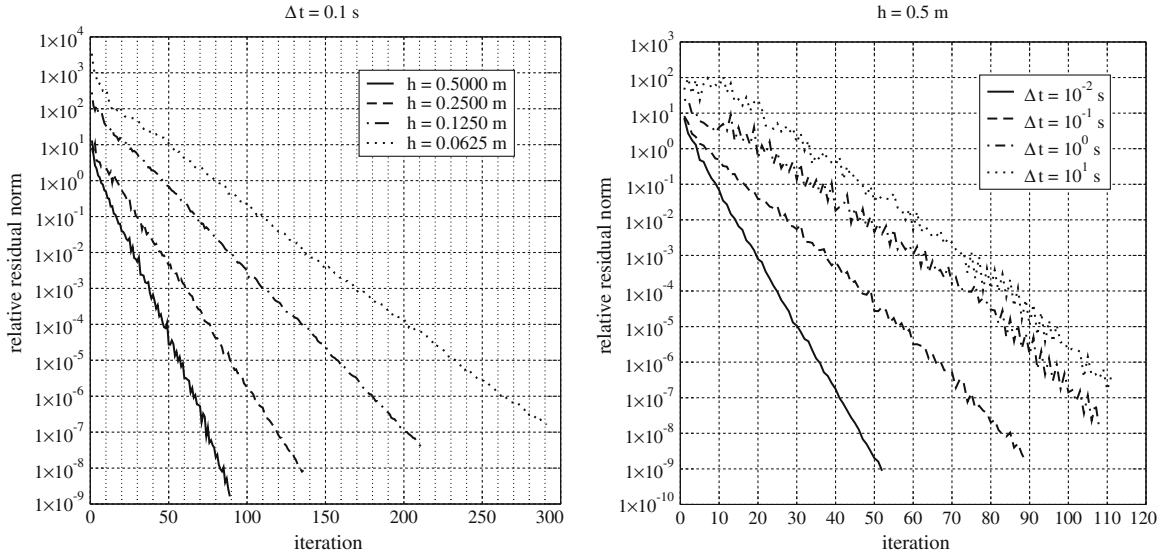

Fig. 9. CP-SQMR convergence profiles varying h with $\Delta t = 0.1$ s (left) and varying Δt with $h = 0.5$ m (right).

cretization error. Similar remarks hold true for the displacements using the L^2-norm of the error (Fig. 8). Consistent with the pore pressure L^∞-norm profile, the theoretical quadratic convergence [23] is progressively lost as h decreases while Δt is kept constant. Fig. 9 shows the relative residual norm:

$$r_r = \frac{\|\mathbf{f}^t - \mathcal{A}\mathbf{z}^{t+\Delta t}\|_2}{\|\mathbf{f}^t\|_2} \tag{53}$$

vs. the number of iterations required by the CP-SQMR algorithm of Appendix A to solve the linear system (31). The different iteration count indicates that the conditioning of $\mathcal{A}$ gets worse as h decreases and Δt increases, which is consistent with the numerical behaviour typically encountered in mixed FE models of subsurface flow [36]. We observe on passing that using the exact factorizations of $\widetilde{S}_1$ and $\widetilde{S}_2$ in Eq. (41), in place of the incomplete Cholesky decompositions, does not provide a significant solver acceleration. For example, in the problem with $h = 0.5$ m and $\Delta t = 0.1$ s convergence is achieved in 88 iterations instead of 113, at the cost of a much larger CPU time spent for the CP computation and application. This may suggest that neglecting the off-diagonal blocks of the Schur complement is the most significant approximation introduced in the CP algorithm.

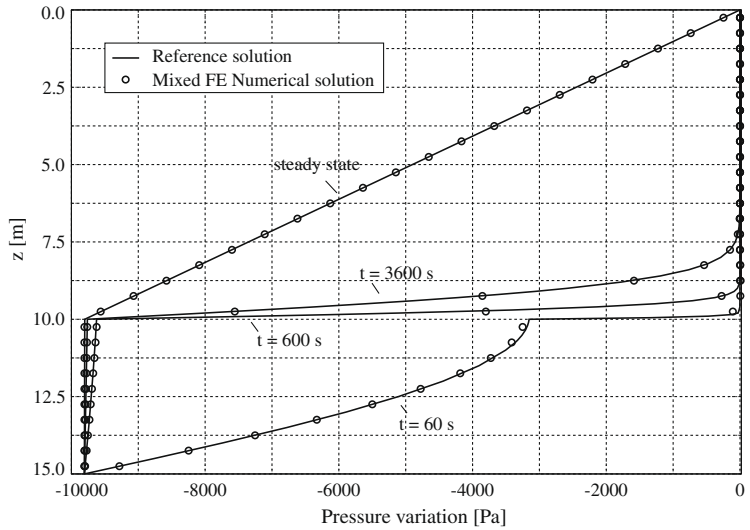

Fig. 10. Heterogeneous consolidation test: reference and mixed FE numerical solutions for the pore pressure.

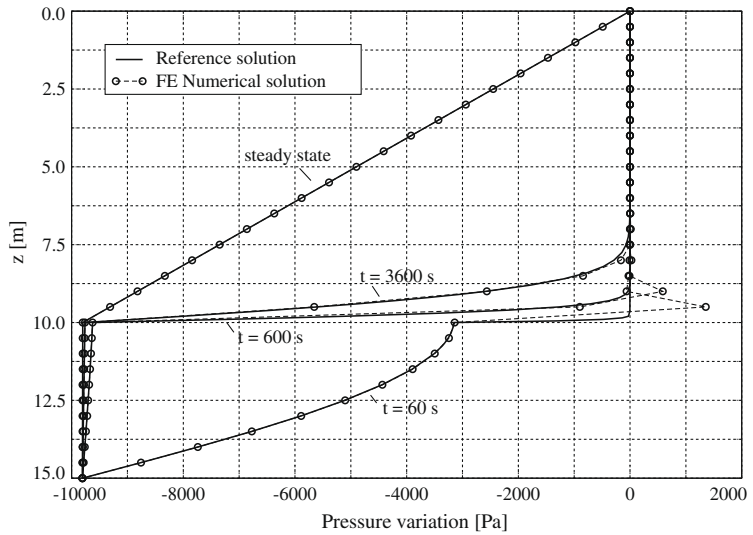

Fig. 11. Heterogeneous consolidation test: reference and standard FE numerical solutions for the pore pressure.

3.2. Comparison with standard FEs

The stability of the numerical solution obtained with the Mixed FE model is investigated in a heterogeneous test problem. The porous column of Fig. 1 is now assumed to consist of 10 m of clay on top and 5 m of sand on bottom. The clay permeability is 1000 times smaller than sand (Table 2) while the elastic properties are the same. Drainage is allowed for also on the bottom boundary where a pore pressure variation of 9810 Pa is prescribed. The top boundary is now traction-free. The computational grid is the same as in Fig. 1.

The simulated pore pressure at different times is shown in Fig. 10. The reference solution has been obtained by progressively refining both the tetrahedral mesh and the time step until convergence. The result used as a reference is obtained with $h = 0.03125$ m and $\Delta t = 0.01$ s. The numerical solution is close to the reference one and appears to be quite stable, with no oscillations at the sand–clay interface. For the sake of a comparison, Fig. 11 provides the pore pressure solution simulated by a standard FE model based on the same mesh and equal order pressure and displacement approximations. Even in this simple problem, standard FEs exhibit pronounced initial pressure oscillations at the sand–clay interface. By contrast, the vertical displacement is stable and accurate in both the FE and mixed FE models (Fig. 12).

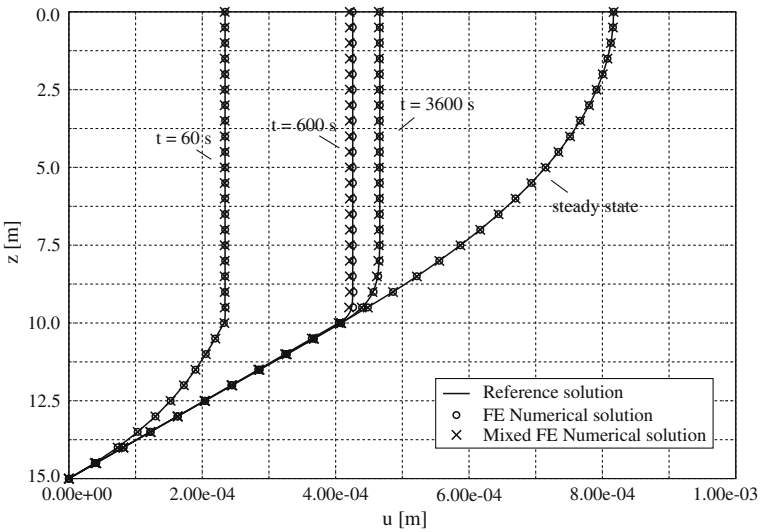

Fig. 12. Heterogeneous consolidation test: reference and numerical solutions for the vertical displacement.

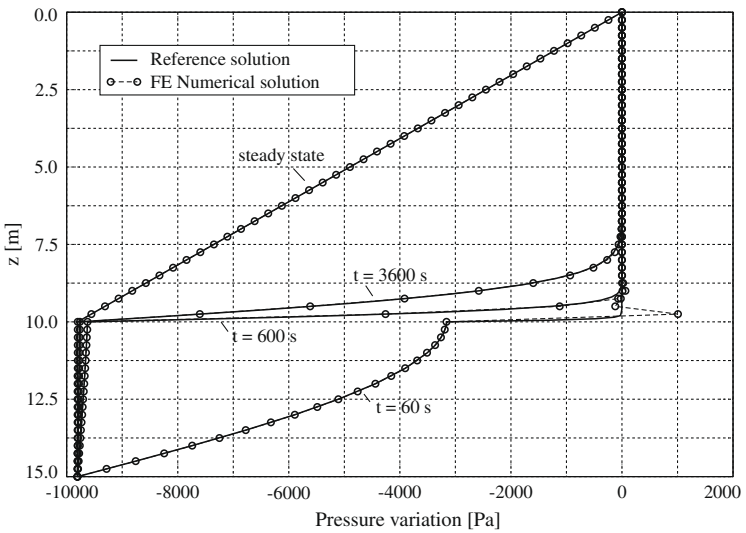

Fig. 13. Heterogeneous consolidation test: reference and standard FE numerical solutions for the pore pressure on a regularly refined tetrahedral mesh so that the total number of unknowns equates that of the mixed FE model.

The stable pore pressure solution provided by the Mixed FE model is obtained at the cost of a larger number of unknowns. To have an idea, the standard FE model has 837 and 279 displacement and pressure unknowns, respectively, while the Mixed FE model totals 837, 720 and 1688 unknowns for displacement, pressure and velocity, respectively, with an overall system

Table 3
Hydro-geological properties of the shallow sediments in the upper Adriatic basin used in the realistic model applications.

	Clay	Silt	Sand
$k_{xx} = k_{yy}$ (m/s)	10^{-7}	10^{-6}	10^{-4}
k_{zz}/k_{xx}	1	1	0.1
ϕ	0.3	0.3	0.3
β (MPa^{-1})	4.32×10^{-4}	4.32×10^{-4}	4.32×10^{-4}
λ (MPa)	1.227	1.227	2.597
μ (MPa)	0.819	0.819	1.732
α	1.0	1.0	1.0

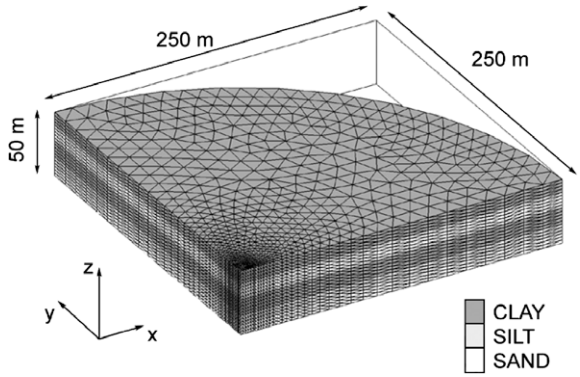

Fig. 14. Axonometric view of the FE grid used in the realistic applications.

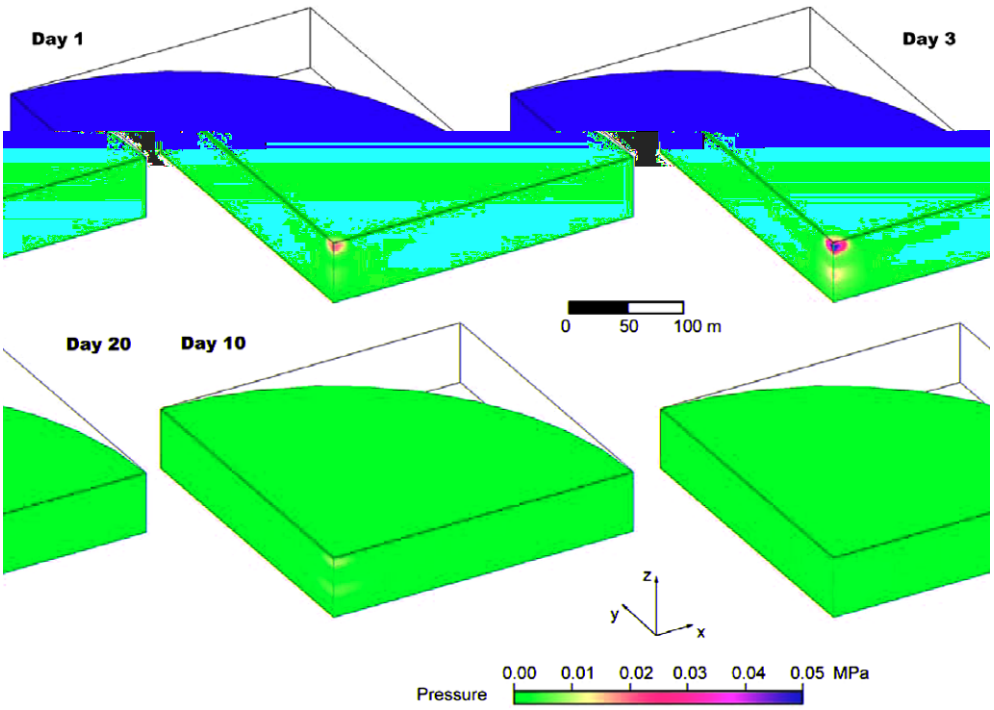

Fig. 15. Test case 1: pore pressure variation vs. time due to the application of a surface load.

size equal to 3245. However, if the tetrahedral mesh is regularly refined so that the standard FE system size is three times larger, oscillations in the pore pressure solution do not vanish, although they are less pronounced than before (Fig. 13). To have practically insignificant oscillations ($\leqslant$50 Pa) the mesh size h at the sand–clay interface must be $\leqslant$0.05 m.

3.3. Realistic applications

The 3-D mixed FE model has been experimented with in two realistic applications addressing the consolidation of a shallow formation in the geological basin underlying the Venice lagoon, Italy. A cylindrical stratified porous volume made of a sequence of alternating sandy, silty and clayey layers down to 50 m depth is simulated. The hydro-geological properties are summarized in Table 3 and are representative of a shallow sedimentary sequence in the upper Adriatic basin [7,37,38]. The axial symmetry of the model geometry allows for the discretization of one fourth only of the overall porous volume (Fig. 14) with zero flux and horizontal displacement prescribed on the inner boundaries. The following additional boundary conditions apply: the outer boundary is fixed and drained, the bottom is fixed and impervious, the top is traction-free and drained. As shown in Fig. 14, a vertically regularly refined grid is used totaling $n_n = 13,356$ nodes, $n_e = 70,080$ elements and $n_f = 143,368$ faces with an overall model size equal to 253,516.

3.3.1. Test case 1: surface load

A uniform surface load distributed over a circular area centered on the domain top with a 10-m radius is applied. The load is set equal to 8 kN/m^2 and is representative of an artificial gravel mound similar to that built at the inlets of the Venice

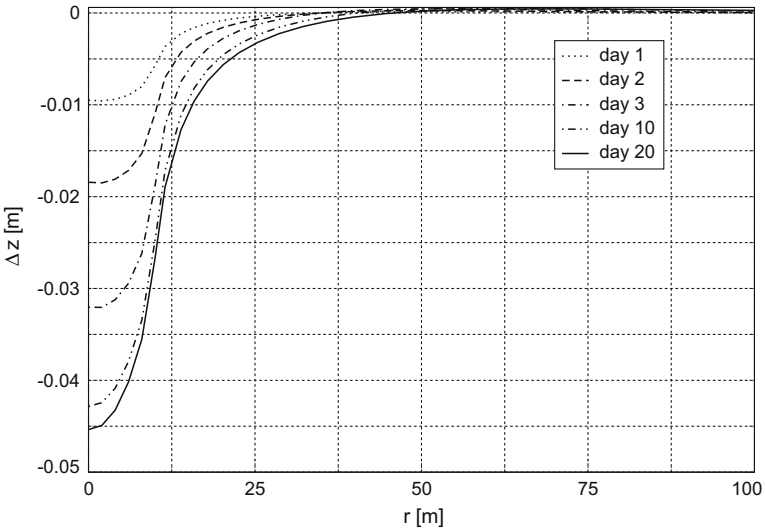

Fig. 16. Test case 1: vertical land displacement vs. time.

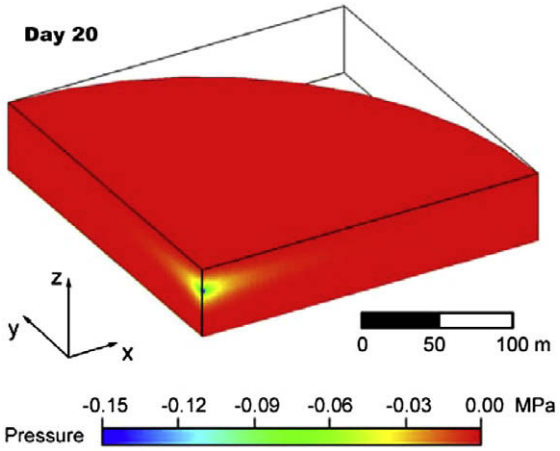

Fig. 17. Test case 2: pore pressure variation 20 days after the start of pumping.

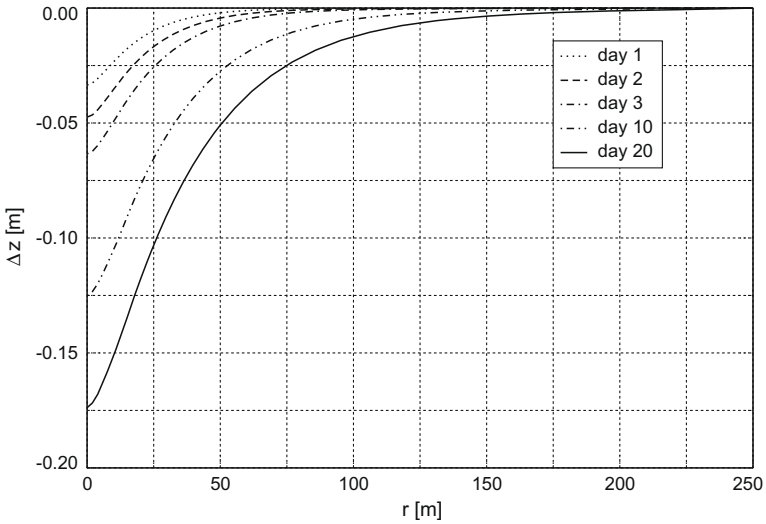

Fig. 18. Test case 2: vertical land displacement vs. time.

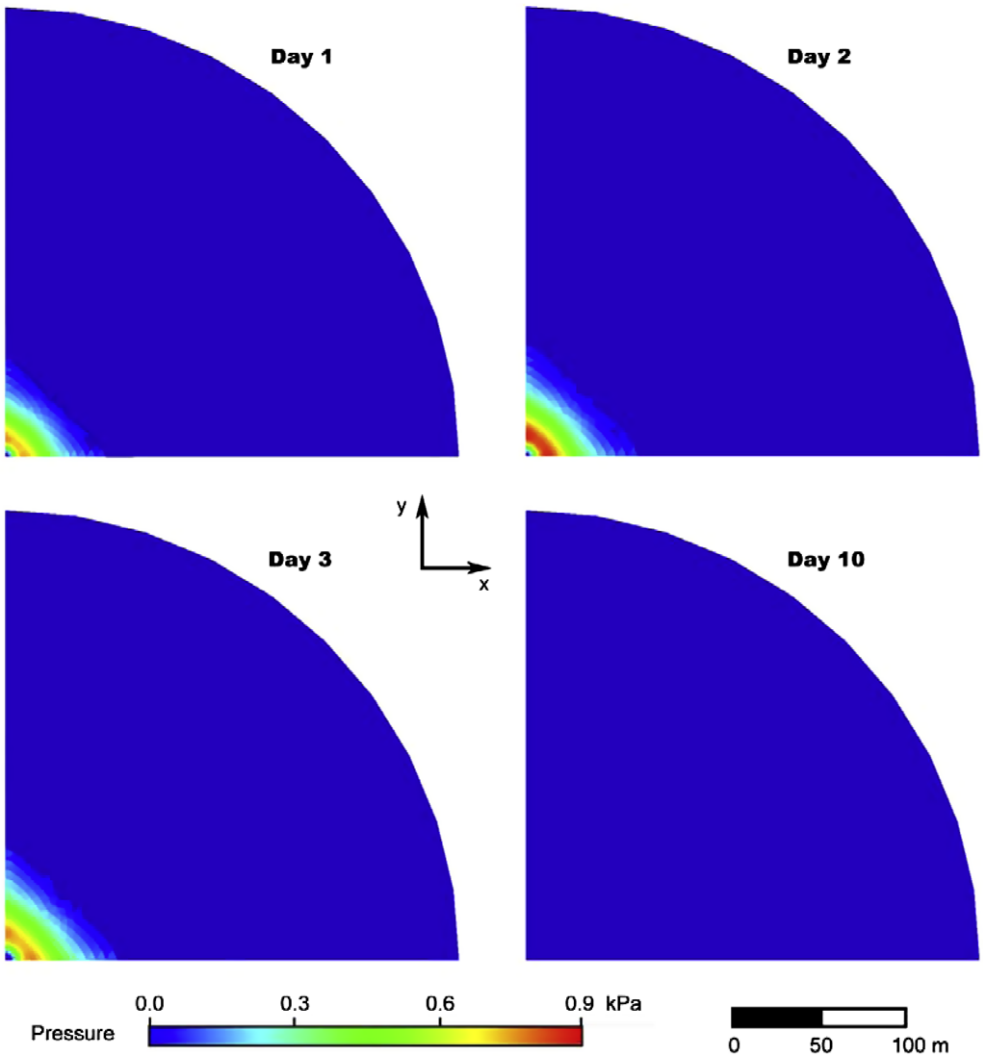

Fig. 19. Test case 2: pore pressure variation vs. time on a horizontal plane located in the middle of the upper clay layer.

lagoon during the MOSE construction, i.e. the mobile barriers planned to protect Venice from the high tides. The load is assumed to increase linearly from 0 to 8 kN/m^2 within 3 days and then to remain constant. As the first layer consists of low permeable sediments, the pore pressure is expected to initially rise at the load application as a consequence of the almost undrained deformation of the clay. The overpressure gradually dissipates in time with a rate depending on the sediment thickness and permeability. This is physically related to the zero volume change rate prescribed at the initial time for the porous medium, which represents the main source of instability in the numerical pore pressure solution. Moreover, the induced overpressure is generally pretty small, so reproducing it numerically may be a difficult task.

The overpressure rise and dissipation in time as simulated by the mixed FE coupled model are shown in Fig. 15. Despite the small overpressure, no oscillations in the numerical solution are observed. Note the pressure rise simulated in the deepest clay layer as well. As the pore water flows out of the top draining surface the soil consolidates and the ground surface subsides. Fig. 16 shows the vertical land settlement vs. time in a radial cross-section. After 20 days the overpressure has almost completely dissipated and the displacement due to the primary consolidation approaches the steady state.

3.3.2. Test case 2: the Noordbergum effect

One of the most known physical processes accounted for by coupling between fluid flow and soil stress is the pressure rise occurring in a low permeable layer confining a pumped formation [39]. The phenomenon is called Noordbergum effect by the name of the village in The Netherlands where it was first observed. Because of the small overpressure involved, especially when pumping occurs at a shallow depth, the Noordbergum effect turns out to be quite difficult to simulate numerically in a stable way.

A constant withdrawal rate of 8×10^{-3} m^3/s is prescribed from the shallowest sandy layer (Fig. 14) through a vertical well located at the centre of the simulated cylindrical porous volume. The pore pressure in the pumped formation achieves a maximum drawdown of 0.15 MPa 20 days after the beginning of pumping. Fig. 17 shows the drawdown distribution, while Fig. 18 provides the related land settlement vs. time along a radial cross-section. To reveal the Noordbergum effect Fig. 19 provides the numerical pore pressure solution as obtained on a 3-m deep horizontal plane, i.e. in the middle of the upper clay layer. As theoretically expected, the pore pressure increases at the initial stage of pumping with a very small value (about 1 kPa, i.e. more than 100 times smaller than the largest drawdown), then quickly dissipates as the consolidation proceeds. The numerical solution appears to be stable with no oscillations and a good degree of symmetry.

4. Conclusions

A fully coupled 3D mixed FE model for the simulation of Biot consolidation has been developed with the aim at alleviating the oscillations of the pore pressure solution along the interface between materials with different permeabilities at the initial stage of the process. A linear piecewise polynomial and the lowest order Raviart–Thomas mixed space are selected to approximate the medium displacement and the fluid flow rate, respectively. The numerical solution is obtained with an algorithm that takes advantage of the block structure of the algebraic linearized system. The numerical model is verified against the well-known Terzaghi's (1-D) and Mandel's (2-D) analytical solutions and then compared to standard FEs. The following results are worth summarizing:

- the mixed FE formulation is element-wise mass conservative and preserves the practical advantage of using low-order interpolation elements for the medium displacement as well;
- the solution algorithm addresses the problem in a fully coupled way, thus improving the stability and avoiding the convergence issues that may arise in a split approach;
- the CP-SQMR algorithm appears to be a robust and efficient tool for the fully coupled solution even though the system conditioning gets worse as the element spacing decreases and the time integration step increases;
- as compared to standard FEs, the mixed FE model appears to be numerically more stable, with no pressure oscillations at the interface between hydrologically heterogeneous media although a coarse discretization and an equally accurate approximation for the displacement are used;
- in realistic large-size settings, the mixed FE model is able to simulate successfully complex coupled processes such as the overpressure within low permeable layers due to a sudden load and the Noordbergum effect.

Acknowledgments

This study has been supported by the Italian MIUR Project (PRIN) "Advanced numerical methods and models for environmental fluid-dynamics and geomechanics". The authors wish to thank two anonymous reviewers for their useful comments and suggestions.

Appendix A. CP-SQMR algorithm

SET $\vartheta_0 = 0,\ \mathbf{d}_0^{(p)} = \mathbf{0},\ \mathbf{d}_0^{(u)} = \mathbf{0},\ \mathbf{d}_0^{(q)} = \mathbf{0}$
CHOOSE $\mathbf{p}_0,\ \mathbf{u}_0,\ \mathbf{q}_0$ ARBITRARILY

$$\mathbf{r}_0^{(p)} = \mathbf{f}^{(p)} - P\mathbf{p}_0 - Q^T\mathbf{u}_0 - \gamma B^T\mathbf{q}_0$$
$$\mathbf{r}_0^{(u)} = \mathbf{f}^{(u)} - Q\mathbf{p}_0 + K\mathbf{u}_0$$
$$\mathbf{r}_0^{(q)} = \mathbf{f}^{(q)} - \gamma(B\mathbf{p}_0 - A\mathbf{q}_0)$$
$$\mathbf{t}_0^{(p)} = P^{-1}\mathbf{r}_0^{(p)}$$
$$\mathbf{t}_0^{(u)} = L_{S1}^{-1}\left(Q\mathbf{t}_0^{(p)} - \mathbf{r}_0^{(u)}\right)$$
$$\mathbf{t}_0^{(q)} = L_{S2}^{-1}\left(\gamma B\mathbf{t}_0^{(p)} - \mathbf{r}_0^{(q)}\right)$$
$$\tau_0 = \sqrt{\|\mathbf{t}_0^{(p)}\|_2^2 + \|\mathbf{t}_0^{(u)}\|_2^2 + \|\mathbf{t}_0^{(q)}\|_2^2}$$
$$\mathbf{w}_0^{(q)} = L_{S2}^{-T}\mathbf{t}_0^{(q)}$$
$$\mathbf{w}_0^{(u)} = L_{S1}^{-T}\mathbf{t}_0^{(u)}$$
$$\mathbf{w}_0^{(p)} = \mathbf{t}_0^{(p)} - P^{-1}\left(Q^T\mathbf{w}_0^{(u)} + \gamma B^T\mathbf{w}_0^{(q)}\right)$$
$$\rho_0 = \mathbf{r}_0^{(p),T}\mathbf{w}_0^{(p)} + \mathbf{r}_0^{(u),T}\mathbf{w}_0^{(u)} + \mathbf{r}_0^{(q),T}\mathbf{w}_0^{(q)}$$
DO $k = 1,\ 2, \ldots$ UNTIL CONVERGENCE
$$\mathbf{s}_k^{(p)} = P\mathbf{w}_{k-1}^{(p)} + Q^T\mathbf{w}_{k-1}^{(u)} + \gamma B^T\mathbf{w}_{k-1}^{(q)}$$
$$\mathbf{s}_k^{(u)} = Q\mathbf{w}_{k-1}^{(p)} - K\mathbf{w}_{k-1}^{(u)}$$
$$\mathbf{s}_k^{(q)} = \gamma(B\mathbf{w}_{k-1}^{(p)} - A\mathbf{w}_{k-1}^{(q)})$$
$$\sigma_k = \mathbf{w}_{k-1}^{(p),T}\mathbf{s}_k^{(p)} + \mathbf{w}_{k-1}^{(u),T}\mathbf{s}_k^{(u)} + \mathbf{w}_{k-1}^{(q),T}\mathbf{s}_k^{(q)}$$
IF $[(\sigma_k = 0)\text{or}(\rho_{k-1} = 0)]$ THEN
  STOP WITH SOLUTION $\mathbf{p}_{k-1},\ \mathbf{u}_{k-1},\ \mathbf{q}_{k-1}$
ELSE
$$\alpha_k = \rho_{k-1}/\sigma_k$$
$$\mathbf{r}_k^{(p)} = \mathbf{r}_{k-1}^{(p)} - \alpha_k\mathbf{s}_k^{(p)}$$
$$\mathbf{r}_k^{(u)} = \mathbf{r}_{k-1}^{(u)} - \alpha_k\mathbf{s}_k^{(u)}$$
$$\mathbf{r}_k^{(q)} = \mathbf{r}_{k-1}^{(q)} - \alpha_k\mathbf{s}_k^{(q)}$$
$$\mathbf{t}_k^{(p)} = P^{-1}\mathbf{r}_k^{(p)}$$
$$\mathbf{t}_k^{(u)} = L_{S1}^{-1}\left(Q\mathbf{t}_k^{(p)} - \mathbf{r}_k^{(u)}\right)$$
$$\mathbf{t}_k^{(q)} = L_{S2}^{-1}\left(\gamma B\mathbf{t}_k^{(p)} - \mathbf{r}_k^{(q)}\right)\ \vartheta_k = \left(\sqrt{\|\mathbf{t}_k^{(p)}\|_2^2 + \|\mathbf{t}_k^{(u)}\|_2^2 + \|\mathbf{t}_k^{(q)}\|_2^2}\right)\Big/\tau_{k-1}$$
$$\psi_k = 1/\sqrt{1+\vartheta_k^2}$$
$$\tau_k = \tau_{k-1}\vartheta_k\psi_k$$
$$\mathbf{d}_k^{(p)} = \psi_k^2\vartheta_{k-1}^2\mathbf{d}_{k-1}^{(p)} + \psi_k^2\alpha_k\mathbf{w}_{k-1}^{(p)}$$
$$\mathbf{d}_k^{(u)} = \psi_k^2\vartheta_{k-1}^2\mathbf{d}_{k-1}^{(u)} + \psi_k^2\alpha_k\mathbf{w}_{k-1}^{(u)}$$
$$\mathbf{d}_k^{(q)} = \psi_k^2\vartheta_{k-1}^2\mathbf{d}_{k-1}^{(q)} + \psi_k^2\alpha_k\mathbf{w}_{k-1}^{(q)}$$
$$\mathbf{p}_k = \mathbf{p}_{k-1} + \mathbf{d}_k^{(p)}$$
$$\mathbf{u}_k = \mathbf{u}_{k-1} + \mathbf{d}_k^{(u)}$$
$$\mathbf{q}_k = \mathbf{q}_{k-1} + \mathbf{d}_k^{(q)}$$
$$\mathbf{v}_k^{(q)} = L_{S2}^{-T}\mathbf{t}_k^{(q)}$$
$$\mathbf{v}_k^{(u)} = L_{S1}^{-T}\mathbf{t}_k^{(u)}$$
$$\mathbf{v}_k^{(p)} = \mathbf{t}_k^{(p)} - P^{-1}\left(Q^T\mathbf{v}_k^{(u)} + \gamma B^T\mathbf{v}_k^{(q)}\right)$$
$$\rho_k = \mathbf{r}_k^{(p),T}\mathbf{v}_k^{(p)} + \mathbf{r}_k^{(u),T}\mathbf{v}_k^{(u)} + \mathbf{r}_k^{(q),T}\mathbf{v}_k^{(q)}$$
$$\beta_k = \rho_k/\rho_{k-1}$$
$$\mathbf{w}_k^{(p)} = \mathbf{v}_k^{(p)} + \beta_k\mathbf{w}_{k-1}^{(p)}$$
$$\mathbf{w}_k^{(u)} = \mathbf{v}_k^{(u)} + \beta_k\mathbf{w}_{k-1}^{(u)}$$
$$\mathbf{w}_k^{(q)} = \mathbf{v}_k^{(q)} + \beta_k\mathbf{w}_{k-1}^{(q)}$$
END IF
END DO

References

[1] K. Terzaghi, Erdbaumechanik auf Bodenphysikalischer Grundlage, F. Duticke, Vienna, 1925.
[2] M.A. Biot, General theory of three-dimensional consolidation, J. Appl. Phys. 12 (1941) 155–164.

[3] O. Coussy, Mechanics of Porous Continua, J. Wiley & Sons, New York, NY, 1995.
[4] W.K.S. Pao, R.W. Lewis, I. Masters, A fully coupled hydro-thermo-poro-mechanical model for black oil reservoir simulation, Int. J. Numer. Anal. Meth. Geomech. 25 (2001) 1229–1256.
[5] M. Ferronato, G. Gambolati, P. Teatini, D. Baù, Radioactive marker measurements in heterogeneous reservoirs: numerical study, Int. J. Geomech. 4 (2004) 79–92.
[6] S. Yin, M.B. Dusseault, L. Rothenburg, Thermal reservoir modeling in petroleum geomechanics, Int. J. Numer. Anal. Meth. Geomech. 33 (2009) 449–485.
[7] P. Teatini, M. Ferronato, G. Gambolati, M. Gonella, Groundwater pumping and land subsidence in the Emilia–Romagna coastland, Italy: modeling the past occurrence and the future trend, Water Resour. Res. 42 (2006), doi:10.1029/2005WR004242.
[8] J. Hudson, O. Stephansson, J. Andersson, C.F. Tsang, L. Ling, Coupled T–H–M issues related to radioactive waste repository design and performance, Int. J. Rock Mech. Mining Sci. 38 (2001) 143–161.
[9] T. Roose, P. Netti, L. Munn, Y. Boucher, R. Jain, Solid stress generated by spheroid growth estimated using a linear poroelastic model, Microvasc. Res. 66 (2003) 204–212.
[10] C. Swan, R. Lakes, R. Brand, K. Stewart, Micromechanically based poroelastic modeling of fluid flow in Haversian bone, J. Biomech. Eng. 125 (2003) 25–37.
[11] M. Ferronato, G. Gambolati, P. Teatini, Ill-conditioning of finite element poroelasticity equations, Int. J. Solids Struct. 38 (2001) 5995–6014.
[12] L. Bergamaschi, M. Ferronato, G. Gambolati, Mixed constraint preconditioners for the iterative solution to FE coupled consolidation equations, J. Comput. Phys. 227 (2008) 9885–9897.
[13] M. Ferronato, G. Pini, G. Gambolati, The role of preconditioning in the solution to FE coupled consolidation equations by Krylov subspace methods, Int. J. Numer. Anal. Meth. Geomech. 33 (2009) 405–423.
[14] M.F. Wheeler, X. Gai, Iteratively coupled mixed and Galerkin finite element methods for poro-elasticity, Numer. Meth. Part. D. E. 23 (2007) 785–797.
[15] S.R. Idelson, J.C. Heinrich, E. Onate, Petrov–Galerkin methods for the transient advective–diffusive equation with sharp gradients, Int. J. Numer. Meth. Eng. 39 (1996) 1455–1473.
[16] P.A. Vermeer, A. Verruijt, An accuracy condition for consolidation by finite elements, Int. J. Numer. Anal. Meth. Geomech. 5 (1981) 1–14.
[17] M.B. Reed, An investigation of numerical errors in the analysis of consolidation by finite elements, Int. J. Numer. Anal. Meth. Geomech. 8 (1984) 243–257.
[18] R.S. Sandhu, H. Liu, K.J. Singh, Numerical performance of some finite element schemes for analysis of seepage in porous elastic media, Int. J. Numer. Anal. Meth. Geomech. 1 (1977) 177–194.
[19] M.A. Murad, A.F.D. Loula, On the stability and convergence of finite element approximations of Biot's consolidation problem, Int. J. Numer. Meth. Eng. 37 (1994) 645–667.
[20] M.A. Murad, A.F.D. Loula, Improved accuracy in finite element analysis of Biot's consolidation problem, Comput. Meth. Appl. Mech. Eng. 95 (1992) 359–382.
[21] M. Tchonkova, J. Peters, S. Sture, A new mixed finite element method for poro-elasticity, Int. J. Numer. Anal. Meth. Geomech. 32 (2008) 579–606.
[22] P.J. Phillips, M.F. Wheeler, A coupling of mixed and continuous Galerkin finite element methods for poroelasticity I: the continuous-in-time case, Comput. Geosci. 11 (2007) 131–144.
[23] P.J. Phillips, M.F. Wheeler, A coupling of mixed and continuous Galerkin finite element methods for poroelasticity II: the discret-in-time case, Comput. Geosci. 11 (2007) 145–158.
[24] P.J. Phillips, M.F. Wheeler, A coupling of mixed and discontinuous Galerkin finite-element methods for poroelasticity, Comput. Geosci. 12 (2008) 417–435.
[25] B. Jha, R. Juanes, A locally conservative finite element framework for the simulation of coupled flow and reservoir geomechanics, Acta Geotech. 2 (2007) 139–153.
[26] R.W. Freund, N.M. Nachtingal, A new Krylov-subspace method for symmetric indefinite linear systems, in: Proceedings of the 14th IMACS World Congress on Computational and Applied Mathematics, 1994, pp. 1253–1256.
[27] J.E. Roberts, J.M. Thomas, Mixed and hybrid methods, in: P.G. Ciarlet, J.L. Lions (Eds.), Handbook of Numerical Analysis, vol. 2, North-Holland, Amsterdam, 1991.
[28] O.C. Zienkiewicz, R.L. Taylor, The Finite Element Method, fifth ed., Butterworth-Heinemann, Oxford, UK, 2000.
[29] K.C. Toh, K.K. Phoon, Comparison between iterative solution of symmetric and non-symmetric forms of Biot's FEM equations using the generalized Jacobi preconditioner, Int. J. Numer. Anal. Meth. Geomech. 32 (2008) 1131–1146.
[30] M. Ferronato, L. Bergamaschi, G. Gambolati, Performance and robustness of block constraint preconditioners in finite element coupled consolidation models, Int. J. Numer. Meth. Eng. 81 (2010) 381–402.
[31] H.F. Wang, Theory of Linear Poroelasticity, Princeton University Press, Princeton, NJ, 2001.
[32] S.J. Wang, K.C. Hsu, The application of the first-order second-moment method to analyze poroelastic problems in heterogeneous porous media, J. Hydrol. 369 (2009) 209–221.
[33] J. Mandel, Consolidation des sols (étude mathématique), Géotechnique 30 (1953) 287–289.
[34] Y. Abousleiman, A.H.D. Cheng, L. Cui, E. Detournay, J.C. Roegiers, Mandel's problem revisited, Géotechnique 46 (1996) 187–195.
[35] L. Cui, A.H.D. Cheng, V.N. Kaliakin, Y. Abousleiman, J.C. Roegiers, Finite element analyses of anisotropic poroelasticity: a generalized Mandel's problem and an inclined borehole problem, Int. J. Numer. Anal. Meth. Geomech. 20 (1996) 381–401.
[36] L. Bergamaschi, S. Mantica, Efficient algebraic solvers for mixed finite element models of porous media flows, in: A.A. Aldama et al. (Eds.), Proceedings of 11th International Conference on Computational Methods in Water Resources, Computational Mechanics and Elsevier Applied Sciences, Southampton, London, UK, 1996, pp. 481–488.
[37] G. Gambolati, P. Gatto, R.A. Freeze, Mathematical simulation of the subsidence of Venice: 2. Results, Water Resour. Res. 10 (1974) 563–577.
[38] G. Gambolati, G. Ricceri, W. Bertoni, G. Brighenti, E. Vuillermin, Mathematical simulation of the subsidence of Ravenna, Water Resour. Res. 27 (1991) 2899–2918.
[39] A. Verruijt, Elastic storage of aquifers, in: R. De Wiest (Ed.), Flow Through Porous Media, Academic Press, New York, NY, 1969, pp. 331–376.